



Kent Academic Repository

New, James S., Kazemi, Bahar, Price, Mark C., Cole, Mike J., Spathis, Vassi, Mathies, Richard A. and Butterworth, Anna L. (2020) *Feasibility of Enceladus plume biosignature analysis: Successful capture of organic ice particles in hypervelocity impacts*. *Meteoritics & Planetary Science*, 55 (8). pp. 1936-1948. ISSN 1086-9379.

Downloaded from

<https://kar.kent.ac.uk/83618/> The University of Kent's Academic Repository KAR

The version of record is available from

<https://doi.org/10.1111/maps.13554>

This document version

Publisher pdf

DOI for this version

Licence for this version

CC BY (Attribution)

Additional information

Versions of research works

Versions of Record

If this version is the version of record, it is the same as the published version available on the publisher's web site. Cite as the published version.

Author Accepted Manuscripts

If this document is identified as the Author Accepted Manuscript it is the version after peer review but before type setting, copy editing or publisher branding. Cite as Surname, Initial. (Year) 'Title of article'. To be published in *Title of Journal*, Volume and issue numbers [peer-reviewed accepted version]. Available at: DOI or URL (Accessed: date).

Enquiries

If you have questions about this document contact ResearchSupport@kent.ac.uk. Please include the URL of the record in KAR. If you believe that your, or a third party's rights have been compromised through this document please see our [Take Down policy](https://www.kent.ac.uk/guides/kar-the-kent-academic-repository#policies) (available from <https://www.kent.ac.uk/guides/kar-the-kent-academic-repository#policies>).

Feasibility of Enceladus plume biosignature analysis: Successful capture of organic ice particles in hypervelocity impacts

James S. NEW ^{*1,2}, Bahar KAZEMI³, Mark C. PRICE², Mike J. COLE², Vassi SPATHIS², Richard A. MATHIES^{1,3}, and Anna L. BUTTERWORTH¹

¹Space Sciences Laboratory, University of California, Berkeley, California 94720, USA

²School of Physical Sciences, University of Kent, Canterbury, Kent CT2 7NH, UK

³Department of Chemistry, University of California, Berkeley, California 94720, USA

*Corresponding author. E-mail: Jamesnew@berkeley.edu

(Received 27 May 2020; revision accepted 10 July 2020)

Abstract—Enceladus is a compelling destination for astrobiological analyses due to the presence of simple and complex organic constituents in cryovolcanic plumes that jet from its subsurface ocean. Enceladus plume capture during a flyby or orbiter mission is an appealing method for obtaining pristine ocean samples for scientific studies of this organic content because of the high science return, reduced planetary protection challenges, and lower risk and expense compared to a landed mission. However, this mission profile requires sufficient amounts of plume material for sensitive analysis. To explore the feasibility and optimization of the required capture systems, light gas gun experiments were carried out to study organic ice particle impacts on indium surfaces. An organic fluorescent tracer dye, Pacific Blue™, was dissolved in borate buffer and frozen into saline ice projectiles. During acceleration, the ice projectile breaks up in flight into micron-sized particles that impact the target. Quantitative fluorescence microscopic analysis of the targets demonstrated that under certain impact conditions, 10–50% of the entrained organic molecules were captured in over 25% of the particle impacts. Optimal organic capture was observed for small particles ($d \sim 5\text{--}15 \mu\text{m}$) with velocities ranging from 1 to 2 km s⁻¹. Our results reveal how organic capture efficiency depends on impact velocity and particle size; capture increases as particles get smaller and as velocity is reduced. These results demonstrate the feasibility of collecting unmodified organic molecules from the Enceladus ice plume for sensitive analysis with modern in situ instrumentation such as microfluidic capillary electrophoresis (CE) analysis with ppb organic sensitivity.

INTRODUCTION

Enceladus has a global water ocean (Postberg et al. 2009; Thomas et al. 2016) that (1) lies under an ice sheet, (2) is in contact with a rocky core (Iess et al. 2014), (3) is understood to have significant salinity (Postberg et al. 2011), and (4) experiences hydrothermal activity at the ocean-core boundary (Hsu et al. 2015; Sekine et al. 2015; Waite et al. 2017). The Enceladus ocean is thought to have significant organic content, which taken together with the geological context suggests high habitability potential (McKay et al. 2008; Glein and Zolotov 2020). Pristine samples from the subsurface ocean are ejected through warm

fractures in the icy crust (Porco et al. 2006; Spencer et al. 2006) forming plumes that extend thousands of kilometers above the surface (Spahn et al. 2006; Lunine 2017). Simple organic compounds have been observed in the plume material (Waite et al. 2006, 2009; Postberg et al. 2008) and, more recently, concentrated and complex macromolecular organics have also been detected (Postberg et al. 2018; Khawaja et al. 2019). Thus, Enceladus presents us with a remarkable opportunity to conduct in-depth astrobiological investigations to probe for organic and bioorganic molecules residing in the subsurface ocean that are indicative of at least habitability but perhaps also extinct or extant life.

Collecting and sensitively analyzing organic samples with minimal alteration during plume transects are becoming increasingly feasible due to recent technical advancements in organic and bioorganic detection instruments. For example, microfluidic capillary electrophoresis (CE) provides sensitive detection of a wide range of relevant organic molecules, including amines, amino acids, and carboxylic acids, with sub-ppb detection limits. The technique was first developed, optimized, and field tested by the Mars Organic Analyzer (MOA; Skelley et al. 2005, 2007; Chiesl et al. 2009) and more recently by the Enceladus Organic Analyzer (EOA; Mathies et al. 2017). The collection of intact molecular biosignatures is also desirable for other techniques including spectroscopy, microscopy, or variants of chromatography-mass spectrometry. Repetitive intact organic capture enables the accumulation of larger plume samples that can be dissolved and transported for analysis in order to increase the detection sensitivity. While typical instruments are capable of operating on a landed mission, the technical advantages of a flyby mission transecting Enceladus' plume, or plumes emanating from other icy bodies, represent a feasible and scientifically valuable format that can be performed faster, at lower cost, and with reduced planetary protection challenges and risk. Direct sampling of the plumes also eliminates the potentially complicating effects of surface processing, radiation exposure (Pavlov et al. 2019), and lander contamination. The capture system must also be compatible with measures to minimize and control for terrestrial contamination and background. This can be achieved by utilizing capture materials such as those considered here that can be rigorously cleaned to sub-ppb levels appropriate for organic analysis.

In a flyby mission, plume particle collection must occur with high efficiency as typical organic analytical instruments have a limit of detection that depends on accumulated bioanalyte concentration. Measurements from Cassini estimate a plume ice column density of approximately $2 \mu\text{L m}^{-2}$ ice at an altitude of 50 km (Porco et al. 2017). Under these conditions, a capture surface with realistic dimensions (10 cm diameter) can achieve ppb biosignature detection limits if the organic capture efficiency is $\sim 50\%$ and multiple passes are integrated as in an Enceladus orbiter. We recently studied hypervelocity polymethyl methacrylate (PMMA) particles impacting metal targets, demonstrating that organic molecules remain chemically intact postimpact and importantly can achieve overall capture efficiencies of $\sim 80\%$ mean residue coverage under these types of conditions (New et al. 2019, 2020). These successful results for organic ice particle simulants provided the basis and encouragement for us to perform hypervelocity impact experiments with ice particles

containing organic molecules as analogs for an Enceladus plume encounter.

A number of previous studies have demonstrated the capture and survival of organic compounds in ice projectiles and targets during hypervelocity impacts of various types. For example, Bowden et al. (2009) observed that organic molecules ejected from ice targets during hypervelocity impacts can survive, but are variably altered or destroyed. Burchell et al. (2014) demonstrated successful transfer of organic compounds from projectile to target during impacts at velocities of ~ 2 and $\sim 4 \text{ km s}^{-1}$. While both experiments indicated that organic molecules can survive hypervelocity impacts under certain conditions, the extent of capture was unquantified and the degree of organic alteration was unknown. Furthermore, the relationships among organic survival (and/or alteration), organic capture efficiency, impact velocity, particle size, and capture medium are unknown for ice projectiles, indicating the critical need for a detailed experimental study of these parameters.

The Stardust mission offers further evidence supporting the capture and survival of organic molecules during particle impacts on aerogels and aluminum foils exposed to the coma of comet Wild 2 with an encounter velocity of 6.1 km s^{-1} . Methylamine and ethylamine, formed on energetically processed icy grains containing ammonia, and approximately equal abundances of methane and ethane were observed in the comet-exposed aerogel (Glavin et al. 2008). Furthermore, the amino acid glycine was detected in several foil samples (Elsila et al. 2009). The detection of these volatile amines and their acid hydrolyzable precursors on the Stardust collector materials suggests that these amines were originally present in submicron particles or icy grains and survived the impact.

Several recent studies attempted to simulate ice particle impacts via laser desorption. Waller et al. (2019) used laser-induced desorption to generate ions and neutrals from a water jet. Klenner et al. (2020) used laser-induced liquid beam ion desorption to heat a water beam and explosively disperse atomic, molecular, and macroscopic fragments. These experiments achieved detection limits of $0.001\text{--}19 \mu\text{M}$ for amino acids in water and $0.2\text{--}23 \mu\text{M}$ for peptides in water. While both methods are suitable for releasing organics from a liquid sample to achieve virtual high velocities into a mass spectrometer source, neither account for the physical mechanics of a real ice particle impact. The phase changes, temperature gradient, and shock profile that occur during ice impacts are complicated and not necessarily replicated by laser desorption.

Our goal here was to apply a direct experimental model to quantitatively study the process of capturing

organics entrained in ice particles using an approach that enables recovery and delivery of sample to a diverse range of analyzers. In this systematic study, ice projectiles doped with organic molecules were impacted into soft metal foil targets at velocities of ~ 1 , 2, and 3 km s^{-1} and their organic capture and survival were quantitatively analyzed. Our objective was to answer three fundamental questions: (1) Do organic molecules entrained in ice particles remain chemically intact during hypervelocity impacts? (2) How does the organic capture and survival depend on particle size? (3) How do the organic capture and survival depend on impact velocity?

EXPERIMENTAL METHODS

Impact experiments were carried out using the two-stage light gas gun (LGG) facility at the University of Kent, UK (Burchell et al. 1999; Hibbert et al. 2017), modified to fire frozen projectiles as described in Fig. 1. We used the “cold gun” to fire cylindrical ice projectiles

that were prepared by pouring a solution into a mold with a volume of $\sim 90 \text{ mm}^3$. The filled mold was then frozen at $-25 \text{ }^\circ\text{C}$. To prevent the projectile from melting while the LGG was set up for firing, the launch tube (where the projectile is placed) and central breech (which connects the launch tube to the first stage of the gun) were cooled to -100 and $2 \text{ }^\circ\text{C}$, respectively. When the gun was ready to be fired, the launch tube and central breech were quickly connected to the rest of the gun and placed on mounts cooled to $-18 \text{ }^\circ\text{C}$ by circulating coolant. The projectile was inserted into the launch tube followed by a frozen four-way split nylon driver sabot, and the gun was fired.

The indium foil targets were positioned in the blast tank normal to the projectile's flight path. The targets were positioned here, and not in the usual target chamber, to increase the number of impacts. The velocity of the projectiles (1.3, 1.7, and 3.1 km s^{-1}) was accurately measured ($\pm 0.05 \text{ km s}^{-1}$) using the driver sabot's time of flight between a laser curtain positioned at the end of the launch tube and a piezoelectric impact

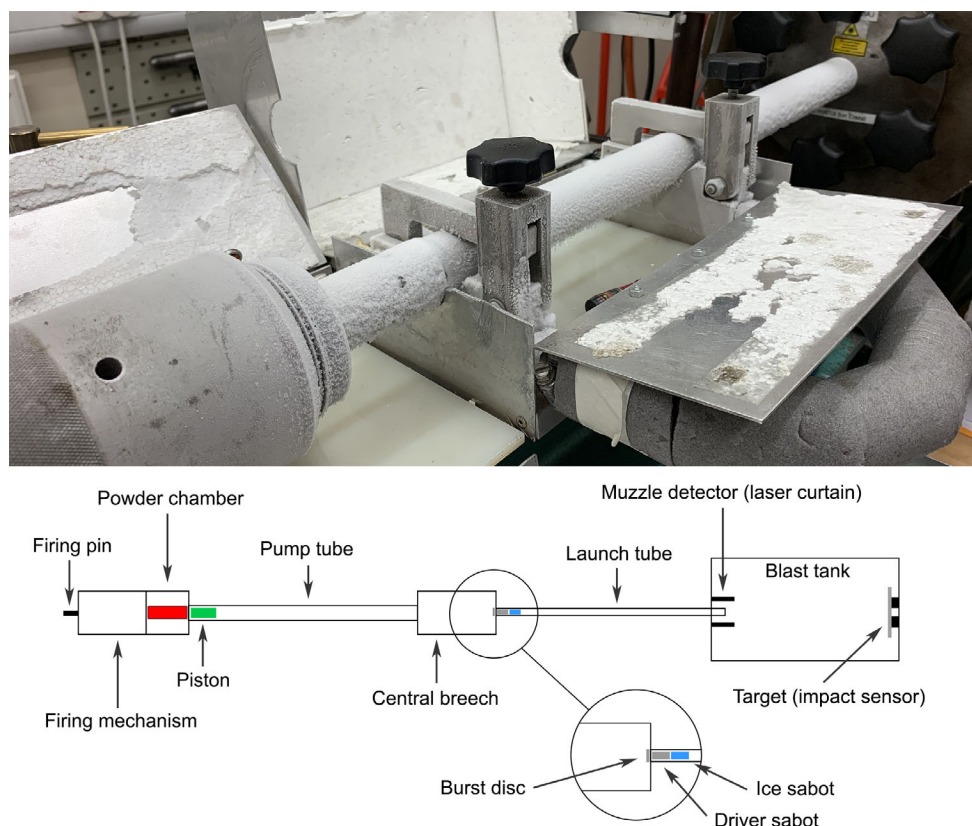


Fig. 1. Photograph (top) and schematic (bottom) of the cold light gas gun (LGG) at the University of Kent. A shotgun cartridge detonates, which drives a piston that compresses a light gas in the pump tube. A thin aluminum disk ruptures at a specific pressure (~ 2 kbar) allowing the compressed gas to accelerate the frozen projectile through an evacuated launch tube. Laser curtains and impact sensors are used to measure the velocity. The target is positioned in the evacuated blast tank. (Color figure can be viewed at wileyonlinelibrary.com.)

sensor on the target. The launch tube and blast tank were pumped down to a vacuum of 50.0 mbar throughout the experiments to prevent slowing of the projectiles due to air resistance and to prevent warming and sublimation of the ice before the impact.

Indium was selected for capture surface (CS) testing as it provides a compliant impact surface that can effectively capture particles while reducing shock and thermal destruction of organic projectiles (New et al. 2019, 2020). Indium is suitable for spaceflight instrument deployment and permits fabrication in a variety of configurations and can be coated onto other materials. Furthermore, indium is readily cleaned to very low levels of organic contamination to reduce background and easily washed to efficiently extract captured organic residue for analysis. Each target consisted of a $10 \times 10 \times 0.2$ mm indium foil (Goodfellow, Catalog #: IN000260/15, Purity: 99.999%) mounted on a thick aluminum disk.

Quantifying the capture of intact organic molecules requires differentiation of the impacting molecules from gunshot residue, which is mainly soot and polyaromatic hydrocarbons (PAH), and from background contamination sources, including previous shot residue, burst disk material, paper impact tracers, and glue. Rather than trying to eliminate all sources of background, we used a unique tracer with high detection specificity and sensitivity. We selected a coumarin fluorophore, Pacific Blue™ (PB, $C_{10}H_4F_2O_7$, molecular mass: 274, Thermo Fisher Scientific), shown with standard IUPAC numbering in Fig. 2. PB has specific wavelength excitation (401 nm) and emission (452 nm) maxima, and fluoresces strongly only when hydrated. Coumarins have a central 1, 2 benzopyrone motif, which itself does not exhibit strong fluorescence. There are over 1000 natural and synthetic coumarins with substitutions at the reactive sites at positions 3, 7,

6, and 8 (Fig. 2; Cao et al. 2019); breaking any of these peripheral bonds will change the fluorescence intensity and wavelength characteristics of the fluorophore. Therefore, only intact PB molecules on the target surface contribute to the captured organic signal. The peripheral bond strengths in PB are more labile than C-C (~ 300 kJ mol⁻¹) or C=C (~ 600 kJ mol⁻¹) bonds in amines, carboxylic acids, or aliphatic side chains of PAHs. For example, the bond dissociation energy of the OH group in 7-hydroxycoumarin is approximately 67 kJ mol⁻¹ (Pérez-González et al. 2012). Furthermore, for stability, PB must be stored cold and as a dry powder; once dissolved, it must be protected from excess light and oxidation. Since organic dyes such as PB are more labile than, for example, amino acids and carboxylic acids, the detection of intact fluorescing PB is a conservative proxy for intact capture of biosignatures such as amino acids and carboxylic acids that may be encountered in the Enceladus plume.

We used a PB succinimidyl ester dye for the preparation of ice projectile solutions and calibration standards; the $C_4H_4NO_2$ imide group is replaced during hydrolysis and does not affect the fluorescence of PB. Detailed calibration methods, defining the fluorescence signal intensity in an epifluorescence microscope field per PB molecule, have been developed to enable quantitative measurements of organic capture (Kazemi, personal communication). The emission quantum yield of PB is pH dependent; therefore, PB stock (10 mM) was diluted in a sodium tetraborate buffer solution (30 mM, pH 9.5) resulting in a 100 μ M PB solution (27 ppm by weight) that was frozen into cylindrical projectiles as imaged in Fig. 2. This mass concentration is approaching the total abundance of organic molecular species thought to be in the Enceladus plume.

The launched ice projectile experiences rapid acceleration and shock fragmentation during the shot

Pacific Blue Structure

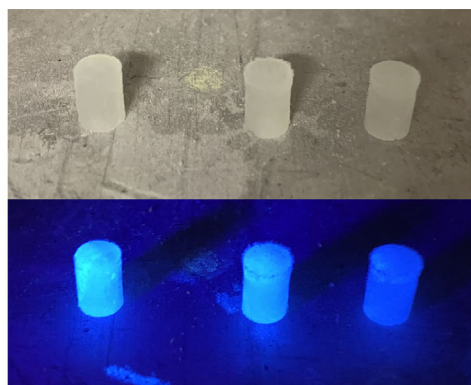
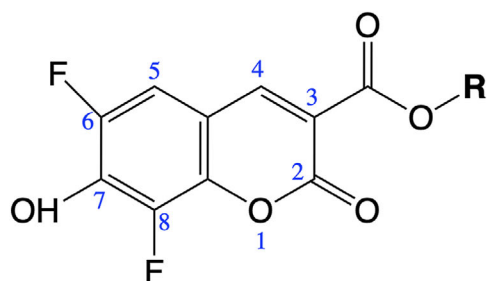


Fig. 2. Pacific Blue™ structure (left). Ice projectiles (diameter 4.3 mm, depth 6.3 mm) illuminated by white light (right, top) and UV light (right, bottom). The blue fluorescence is due to the Pacific Blue™ dye in the ice solution. (Color figure can be viewed at wileyonlinelibrary.com.)

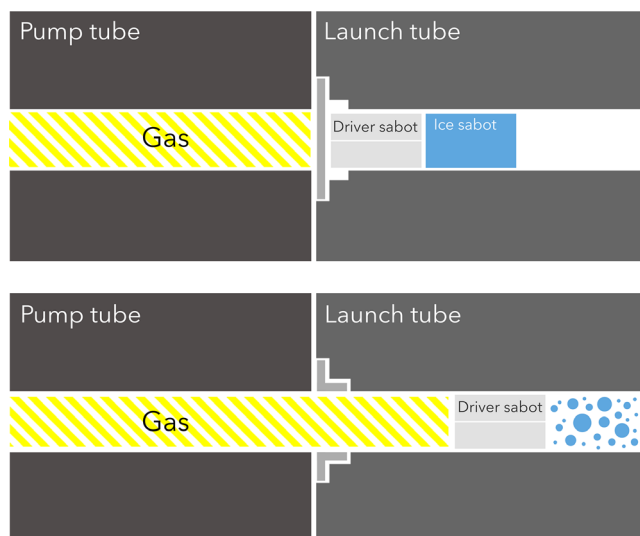


Fig. 3. Schematic of the ice projectile and driver sabot positioned in the launch tube (top). When the burst disk ruptures, the gas and driver sabot accelerate the fragmented ice particles through the launch tube (bottom). The driver sabot ensures that all ice particles travel at a similar velocity and act as a thermal barrier between the ice and the hot compressed gas. (Color figure can be viewed at wileyonlinelibrary.com.)

(Fig. 3) resulting in a plume of ice particles, with diameters ranging several μm to mm , that proceed to the target and form impact craters. Observations indicate that the largest plume particles at Enceladus have diameters ranging 2–6 μm at an altitude of 50 km (Hedman et al. 2009). The shock fragmentation process enables us to produce significant numbers of small particles (<15 μm), replicating similar impacts expected to occur on a capture surface during an Enceladus plume transect. While this is the desired outcome, the fragmentation admits gas flow through the projectile plume resulting in variations in individual particle velocities. Therefore, a four-way split plastic driver sabot (that is discarded in the blast tank) was positioned behind the ice projectile to produce a more uniform velocity. Additionally, the driver sabot acts as a thermal barrier between the ice projectile and the hot compressed gas.

ANALYSIS METHODS

Crater analysis was carried out on over 270 craters formed by particles with diameters ranging between 5 and 70 μm for impacts on indium foils in the 1–3 km s^{-1} velocity range. The analysis can be broken down into three sequential steps. (1) Bright-field and epifluorescence image acquisition of impact craters, (2) image processing for crater dimensions and residue quantitation, and (3) organic capture efficiency

calculations. Although we use epifluorescence microscopy as a quantitative analysis method here, during an Enceladus plume-sampling mission, our analysis approach is to dissolve all the captured material and efficiently transport it to concentration-based chemical analyzers such as the EOA (Mathies et al. 2017).

A Nikon Eclipse E800 epifluorescence microscope with a 5 Megapixel Media Cybernetics Evolution MP CCD camera was set up to acquire images of craters on the indium foils. A mercury light source was used to epi-illuminate and excite the samples with a 410 nm band-pass filter and the emission was detected with a 435 nm long-pass filter. A Plan 10x/0.25 Nikon objective lens was used for image acquisition that enabled visualization and quantitation of craters with diameter $\geq 10 \mu\text{m}$. Exposure times of 1 and 10 seconds were applied while acquiring the bright-field and fluorescence images, respectively.

The fluorescence of Pacific Blue™ (PB) is humidity dependent: PB has weak emission when fully dehydrated but its emission intensifies dramatically when humidified. A humidity of 70% was identified as providing optimal fluorescence while preventing condensation on the foils. The foils were positioned in an enclosed sample chamber with two gas inlets for humidity control. Dry nitrogen gas was pumped through the sample chamber to reduce the humidity (<10%) and acquire bright-field and background fluorescence images. Humid air (70%) was then introduced with a 3.5 L min^{-1} flow rate and additional fluorescence images were acquired. Further details of the analysis apparatus and method will be presented in an upcoming publication.

The images were processed and analyzed with ImageJ (Abràmoff et al. 2004) using the following method. Craters of interest were located using the bright-field images and their regions of interest (ROI) were identified as illustrated in Fig. 4A. Ice craters were identified via typical crater features such as indentations on the capture surface, defined edges, protruding rims, and absence of foreign artifacts. To eliminate false positives, small craters that were close to the visual limit of the objective lens and at the lower threshold resolution of the CCD camera were verified through the microscope viewfinder. This allowed us to distinguish small craters from background noise and validate the bright-field observations. The ROI were then used to measure the area and major/minor diameters of craters from an elliptical fit. Defining the exact ROI is subjective and can lead to uncertainties in crater measurements. To quantitate these measurements, we outlined a small (11.8 μm) and a large (97.3 μm) crater multiple times with different methods (i.e., outer rim,

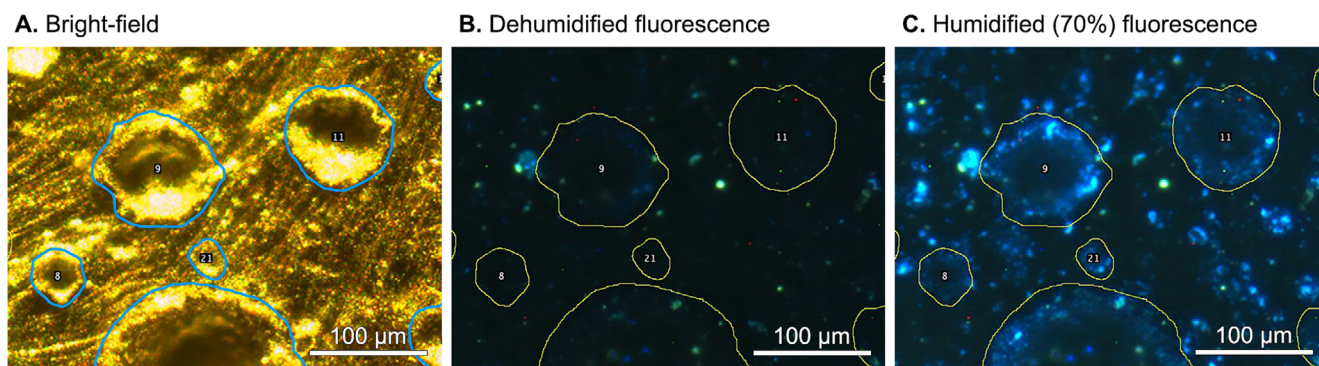


Fig. 4. A) Bright-field image showing craters with regions of interest (ROI) outlined. B) Dehumidified fluorescence image showing background fluorescence, artifacts, and weak PB emission in craters. C) Humidified (70%) fluorescence image showing craters with intense PB emission. (Color figure can be viewed at wileyonlinelibrary.com.)

inner rim, central rim, exact, and smooth lines) and found that the standard deviation in the diameter measurements was approximately $1.5 \mu\text{m}$ (12.7%) for the small crater and $3.5 \mu\text{m}$ (3.6%) for the large crater. Although the percentage uncertainty decreased for large craters, their absolute uncertainty increased due to greater variation in crater morphology. Unlike small craters that have flat, defined edges and comparable shapes that are readily measurable, large craters form protruding rims. As a systematic method was applied to the ROI outlining, we expect these uncertainties to be an upper limit and not significant in the calculation of the final capture efficiency results. The low humidity fluorescence images, as seen in Fig. 4B, were used to identify fluorescent background artifacts. Only signals that increased significantly upon humidification, represented in Fig. 4C, were analyzed as valid PB signals revealing the capture of chemically intact organic molecules. The fluorescence images were stacked and split into their RGB components and the surplus red and green channels were discarded. The original ROI were superimposed onto the blue channel image and the mean fluorescence intensity (counts/s) within the craters was measured. Finally, the mean intensities of 3 PB-free regions in the vicinity of the craters were measured and used to subtract the background intensity.

The organic capture efficiency was calculated as the percentage of organic molecules in the impacting particle that were detected on the foil in the ROI. Projectile fragmentation is a random process; thus, it was necessary to determine the size of the ice particle for each impact based on the crater dimensions. New et al. (2019, 2020) used PMMA particles with well-defined dimensions to study the relationships among particle size, impact velocity, and crater dimensions for indium-foil impacts as well as other capture surfaces.

Since PMMA has a similar melting point relative to thermal shock ($160 \text{ }^\circ\text{C}$) and density (1.18 g cm^{-3}) to ice, this calibration enabled us to convert the mean observed crater diameter into the predicted impact particle diameter. A natural variation of 6.5% (mean standard deviation) was observed in the sample craters formed by the PMMA impacts. The volumes of impacting ice particles were calculated assuming spherical fragmentation. This allowed us to directly use the PMMA calibration and provided a conservative capture estimate as spherical particles represent the maximum expected particle volume. The numbers of PB molecules in the impacting particle were then determined based on the concentration of PB in the ice particle solution ($1 \times 10^{-4} \text{ mol/L}$) and the particle volume ($\pm 20\%$).

The fluorescence intensity per PB molecule on the target surface was calibrated using a suite of PB concentrations in 30 mM sodium tetraborate buffer solutions. Briefly, 50 nL drops of PB-borate solution were deposited on aluminum foils using a custom microarray spotter with PB concentrations ranging from 0.01 to $10 \mu\text{M}$. The intensity of the dried and then re-humidified droplets was measured at 70% humidity using the epifluorescence microscope. The molecular concentration was plotted against the mean intensity (counts/s) of the integrated droplet and used to determine the number of fluorescent counts per second per PB molecule. A power function ($y = ax^b$) was fit to the data for quantitation where $a = 2.8 \times 10^7$ (0.28% uncertainty) and $b = 8.6 \times 10^4$ (0.36% uncertainty). A more detailed account of this method, the results, and the calibration curves will be presented in an upcoming publication (Kazemi, personal communication). The number of intact PB molecules that were captured within a crater ROI was then determined by multiplying the mean intensity per unit area by the ROI area and

then dividing by the determined counts per second per PB molecule. Finally, organic capture was calculated from the ratio of the number of PB molecules detected in the crater ROI to the number of PB molecules in the impacting particle.

Thus, accounting for the uncertainty propagation in our multistep calculations, originating from the deviation of data points in the crater versus particle size calibrations, particle shape, PB fluorescence calibrations, and ROI selection, we expect our final capture efficiency results to have approximately 20% relative uncertainty (e.g., 10% capture efficiency would be $10 \pm 2\%$).

RESULTS

PB molecules were readily detected by epifluorescence microscopy on the humidified indium foils for the 1–2 km s⁻¹ velocity impacts indicating successful organic capture and survival. The bright-field images in Fig. 5 show a representative small and large crater for impact velocities of 1.3 and 1.7 km s⁻¹. The fluorescence images in Fig. 5 exhibit visible PB emission in the craters which can be used to quantitate organic capture efficiency based on the particle diameter determined from the craters in the bright-field images. The two forms of PB residue capture observed were: (1) crater residue located within well-defined craters and (2) surface residue situated between craters. High-resolution crater identification was performed through the viewfinder of the microscope as it was difficult to differentiate between small craters and surface residue in the bright-field images alone. Explanations for the origins of both residue types are considered in the Discussion section.

Similar bright-field and fluorescence images in Fig. 6 show a representative crater formed by a 4 μm

diameter particle with a 3.1 km s⁻¹ velocity impact. At this higher impact velocity, the visible signs of PB were less obvious in the dehumidified and humidified fluorescence images. Detailed intensity analysis of craters in the CCD images, however, demonstrated that trace amounts of organic molecules entrained in small particles ($d \leq 10 \mu\text{m}$) were deposited on the foil and remained chemically intact at 3.1 km s⁻¹.

The capture efficiencies (%) of organic molecules are shown plotted against particle diameter (μm) in Fig. 7 for over 270 impact events with velocities from 1 to 3 km s⁻¹. The data presented here focus on particles with diameters up to 70 μm. Analysis of larger particles was beyond the scope of this work and required additional calibration. A logarithmic scale is used to display the organic capture efficiency for all data points over this four-decade range. All data points and their calculated values are plotted in Fig. 7; however, organic capture efficiencies <0.5% are within 1-sigma standard deviation of background noise and are therefore not distinguishable from zero capture. The background noise is depicted by the shaded region in Fig. 7 and was calculated by averaging the intensity of 10 background ROI. At a velocity of 1.3 km s⁻¹, organic capture efficiency rises from ~1% at 70 μm to approximately ~3% at 15 μm with a maximum of $30.5 \pm 6.1\%$ recorded for a $12.5 \pm 0.8 \mu\text{m}$ diameter particle. For 1.7 km s⁻¹ velocity impacts, the organic capture efficiency rises from ~2% at 50 μm to ~7% at 10 μm with a maximum of $49.2 \pm 9.8\%$ recorded for an $8.5 \pm 0.6 \mu\text{m}$ diameter particle. At a velocity of 3.1 km s⁻¹, the data are sparse with effectively zero organic capture (<0.5%) recorded for the majority of impacts. Several small particles ($d < 10 \mu\text{m}$) exhibited capture above background with a maximum of $11.0 \pm 2.2\%$ recorded for an $8.9 \pm 0.6 \mu\text{m}$ diameter particle.

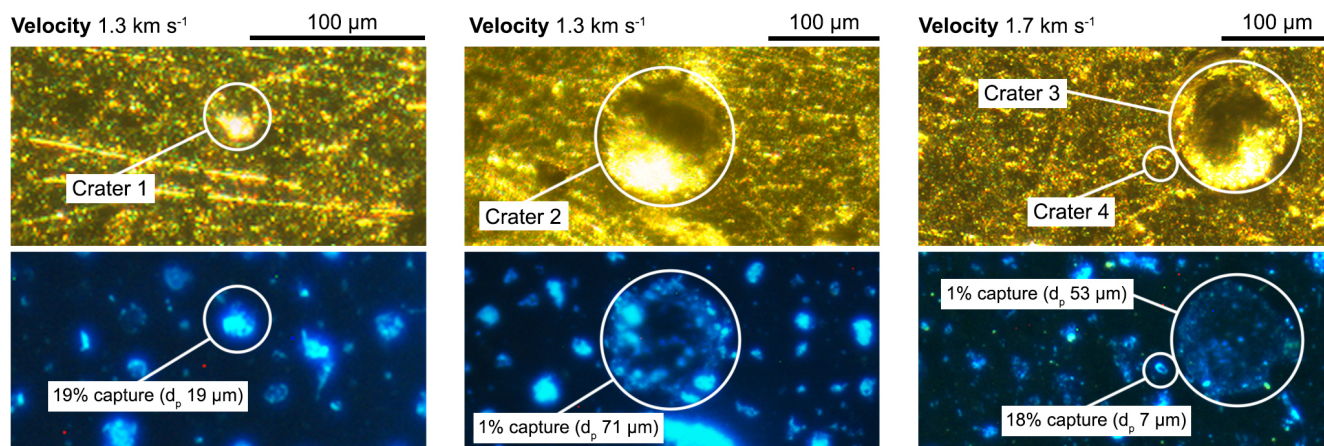


Fig. 5. Bright-field and humidified fluorescence images of craters on indium foils from 1 to 2 km s⁻¹ velocity impacts. Fluorescing PB residue is observed in the circled craters and the corresponding particle diameters and organic capture efficiencies are indicated. Craters were validated by visual microscopic examination to eliminate false positives.

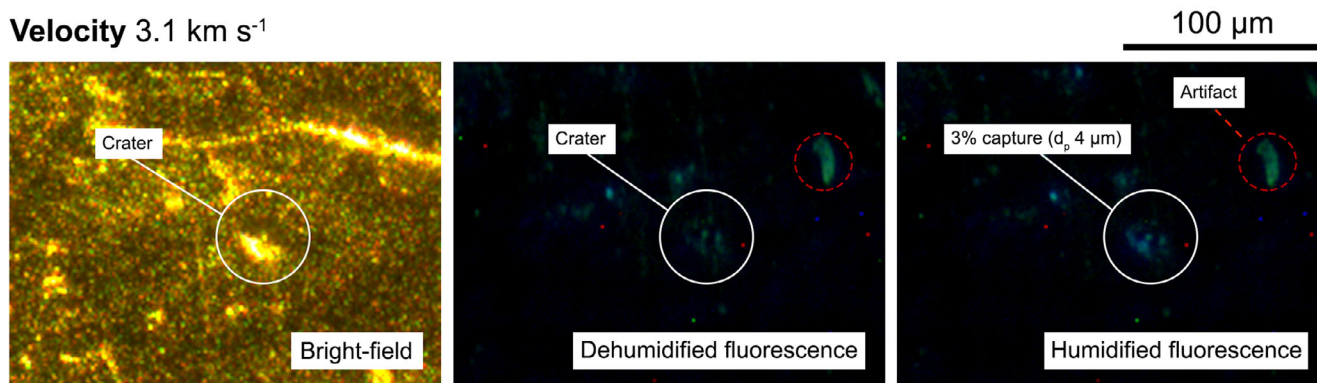


Fig. 6. Bright-field and (dehumidified/humidified) fluorescence images of a representative crater on indium foil formed by a $4\ \mu\text{m}$ diameter particle with a $3.1\ \text{km s}^{-1}$ velocity. Trace amounts of PB residue are observed in the crater (circled) in the humidified fluorescence image. A representative artifact is circled in red. (Color figure can be viewed at wileyonlinelibrary.com.)

Power functions were fitted to the organic capture efficiency data and are depicted by the dashed red lines in Fig. 7. The 1.3 and $1.7\ \text{km s}^{-1}$ data sets are sufficiently populated to define power law fits with exponents of -0.7 and -1.1 , respectively. The $3.1\ \text{km s}^{-1}$ data set is more scattered and the majority of the impacts registered organic capture below the background noise threshold (shaded region). For completeness, we plotted the power function for $3.1\ \text{km s}^{-1}$ data, which gives an exponent of -0.9 ; however, this is not well defined by the data. These fits were performed to enable estimations of capture for smaller particles and to test simple models for the organic capture mechanism (see the Discussion section).

For further comparison, the organic capture efficiency data were grouped into $5\ \mu\text{m}$ particle diameter size bins and presented in Fig. 8 where boxplots display the median (solid orange line), mean (green triangle), interquartile range (IQR), and outliers (open circles) based on Tukey's method ($1.5\ \text{IQR}$). For the $1.3\ \text{km s}^{-1}$ experiments, the median rises from $1.0 \pm 0.2\%$ to $2.6 \pm 0.5\%$ and the mean rises from $1.2 \pm 0.2\%$ to $7.7 \pm 1.5\%$, as the particle size decreases to $10\text{--}15$ microns. For the $1.7\ \text{km s}^{-1}$ experiments, the median rises from $1.2 \pm 0.2\%$ to $7.2 \pm 1.4\%$ and the mean rises from $1.3 \pm 0.3\%$ to $10.5 \pm 2.1\%$, as the particle size decreases to $5\text{--}10$ microns. At $3.1\ \text{km s}^{-1}$, the median organic capture efficiencies for all impacts ($0.01\text{--}0.25\%$) were on the order of the background noise and the highest mean organic capture ($1.3 \pm 0.3\%$) was in the $5\text{--}10\ \mu\text{m}$ diameter bin. At $3.1\ \text{km s}^{-1}$, particles were concentrated in the $d < 30\ \mu\text{m}$ diameter range due to greater fragmentation on acceleration, leading to a very small number of large particles.

In order to better consider our results in the context of an Enceladus plume encounter, we focus on the

smallest diameter bin with data for each velocity. The $10\text{--}15\ \mu\text{m}$ diameter bin at $1.3\ \text{km s}^{-1}$ had a median capture efficiency of $2.6 \pm 0.5\%$ and a mean of $7.7 \pm 1.5\%$ with a maximum capture efficiency of $30.5 \pm 6.1\%$. The $5\text{--}10\ \mu\text{m}$ diameter bin at $1.7\ \text{km s}^{-1}$ had a median of $7.2 \pm 1.4\%$ and a mean of $10.5 \pm 2.1\%$ with a maximum capture efficiency of $49.2 \pm 9.8\%$. The $0\text{--}5\ \mu\text{m}$ diameter bin at $3.1\ \text{km s}^{-1}$ had a capture median of $0.1 \pm 0.02\%$ (i.e., consistent with background) and a mean of $0.8 \pm 0.2\%$ with a maximum capture efficiency of $3.2 \pm 0.6\%$. Capture efficiencies greater than 10% were detected in over a quarter of all craters formed by small particles ($<10\ \mu\text{m}$) with velocities between 1 and $2\ \text{km s}^{-1}$.

DISCUSSION

Our experiment is the first to directly perform the exact ice particle impacts anticipated in an Enceladus-plume transect. The data presented here are critical to the selection of mission flyby and orbital conditions for nondestructive biosignature capture and analysis at Enceladus and other solar system locations. Ultimately, experiments of this type should enable predictions of the amount of captured ice in a flyby mission and of the science measurement capabilities of various instruments using these samples.

The results presented in Figs. 7 and 8 demonstrate that an indium CS can effectively capture intact organic molecules entrained in ice particles during high-velocity impacts ranging from 1 to $2\ \text{km s}^{-1}$. High organic capture efficiency ($\sim 50\%$) is observed for some impacts, with capture efficiencies greater than 10% detected in over a quarter of all craters formed by small particles ($<10\ \mu\text{m}$). This result is encouraging as orbital dynamics models indicate that plume encounter velocities of $1\text{--}2\ \text{km s}^{-1}$ are feasible from a Saturn orbit, and we can

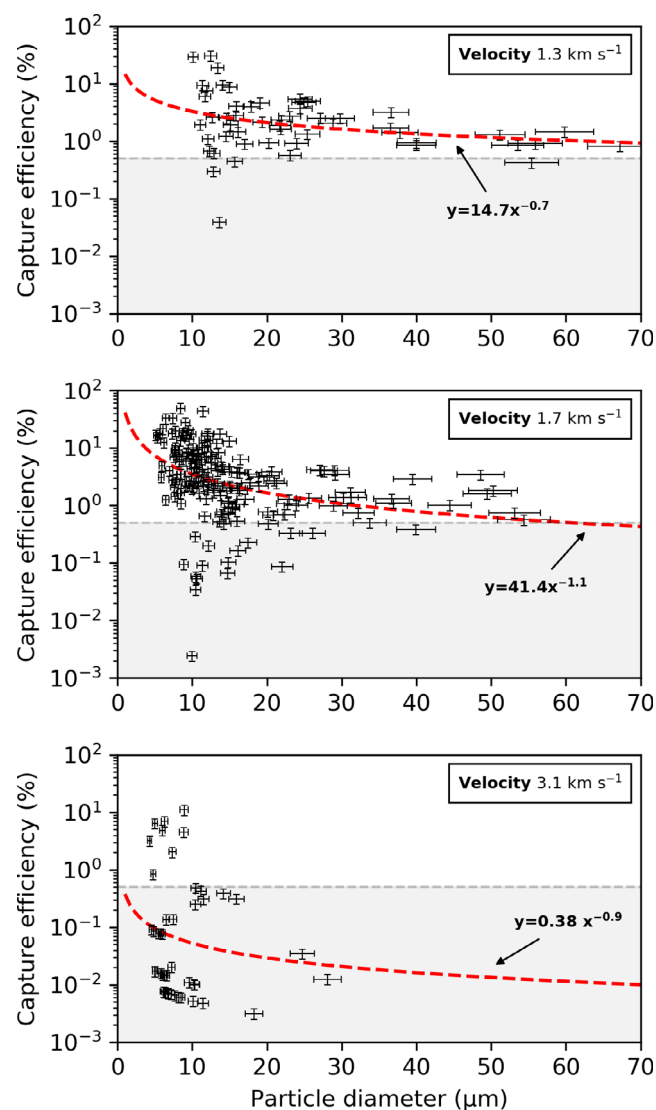


Fig. 7. Organic capture efficiency (%) plotted on logarithmic scale against particle diameter (μm) for impacts at 1.3 ($N = 54$), 1.7 ($N = 173$), and 3.1 ($N = 45$) km s^{-1} . Power functions fit to the organic capture efficiency data are represented by the dashed red line to enable extrapolation to smaller particle sizes and to test possible impact models. The shaded regions represent the background noise for all velocities. Derivation of errors is discussed in the text. (Color figure can be viewed at wileyonlinelibrary.com.)

therefore expect to capture sufficient quantities of organic material with a single or multi-orbit mission. Defining the optimal organic capture velocity based on these data is challenging due to the range of capture efficiencies, particularly for small particles. Thus, we grouped the data into $5 \mu\text{m}$ size bins (Fig. 8) focusing on the smallest size range for each velocity to emulate Enceladus-plume particles. To assess the overall trend of the data, we consider the median organic capture efficiency to avoid mean bias toward low frequency

high-capture or low-capture outliers (Fig. 8). The results imply that organic capture efficiency for an indium CS peaks at the lowest velocities and smallest particles achieved in our experiments. Since organic capture depends on particle size as well as velocity, we may expect the optimum capture velocity to be larger for smaller particle sizes.

A rapid decrease in organic capture efficiency was observed above the optimal ($1\text{--}2 \text{ km s}^{-1}$) capture velocity range, with the median capture efficiency falling into the background noise for 3.1 km s^{-1} velocity impacts. In high-velocity impacts, the particles carry additional kinetic energy, which leads to increased high-speed ejecta (Eichhorn 1978) resulting in the observed drop in organic capture. It will be useful to explore different capture surfaces that alter the energy partition on impact to reduce particle disruption and ejecta at high velocities. Although more data are needed, especially for small particles, the current results indicate that low-velocity plume transects at lower than $\sim 3 \text{ km s}^{-1}$ are the best choice for efficient sampling of unmodified organic molecules using indium capture surfaces. To recap, a positive identification of PB on our capture surface represents the capture of unaltered PB molecules. Thus, this experiment presents a conservative estimate of intact organic capture.

It is evident from the results presented in Fig. 7 that, for all velocities, organic capture efficiency is significantly higher for small particles and there is a consistent increase of capture with decreasing particle size. We hypothesize that the amount of captured organic material is proportional to the impact surface area of the particle, which scales with the diameter squared. Our data also demonstrate that higher kinetic energy impacts have reduced material deposition suggesting that organic capture is inversely proportional to kinetic energy, which scales with the mass of the particle or the diameter cubed at fixed velocity. This hypothesis predicts that the organic capture efficiency is inversely proportional to the diameter and should fit a power function of the form $y = ax^b$, where y is the organic capture efficiency, x is diameter, a is a fitting parameter, and b is approximately -1 . While there is a convincing correlation between the data and power functions for the $1\text{--}2 \text{ km s}^{-1}$ velocity impacts in Fig. 7, a wider distribution at 3.1 km s^{-1} is observed, which is likely due to the low signal-to-background-noise ratio and the sparsity of events. The fits reveal exponents of -0.7 , -1.1 , and -0.9 for the 1.3 , 1.7 , and 3.1 km s^{-1} velocity impacts, respectively. Thus, the data correlation together with the exponents of approximately -1 indicates that this model is a reasonable first approximation again indicating that there is an increase in organic capture efficiency as the particle diameter decreases.

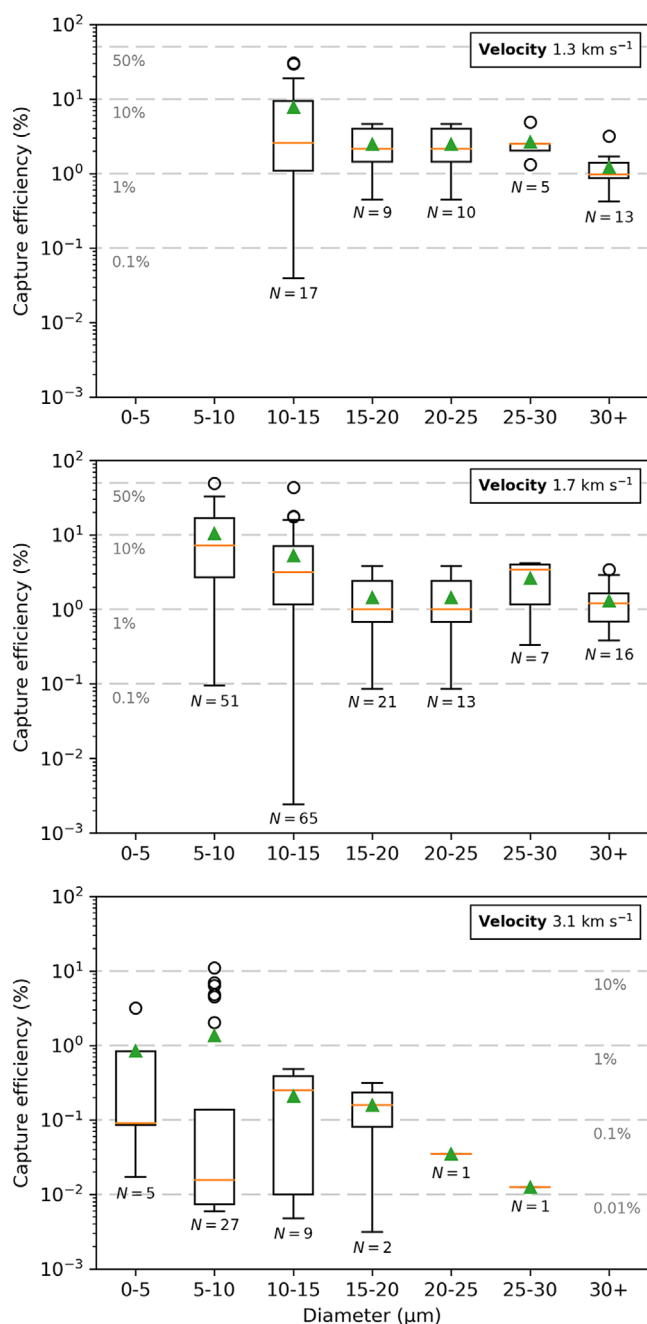


Fig. 8. Boxplots summarizing the organic capture efficiency data in particle diameter bins for impacts at 1.3, 1.7, and 3.1 km s⁻¹. The solid orange line represents the median, the green triangle represents the mean, and the outliers (open circles) are defined by Tukey's method (1.5 IQR). (Color figure can be viewed at wileyonlinelibrary.com.)

To further this analysis, we plotted the logarithm of organic capture efficiency against the logarithm of the particle diameter in Fig. 9. A linear function (black line) with confidence bands (green) based on a 0.05 significance level was fitted to the data to extrapolate

the organic capture efficiencies to smaller particles with diameters representative of the Enceladus plume. The greatest mass density of plume particles, at an altitude of 50 km, resides in 4–6 μm diameter particles (Hedman et al. 2009). For this size range relevant for Enceladus, we estimate the organic capture efficiency for a 1.3 km s⁻¹ encounter velocity to be greater than 2–9% and for a 1.7 km s⁻¹ encounter velocity greater than 4–9%.

Our previous studies suggested that particles can rebound off the capture surface at low velocities leading to reduced capture (New et al. 2019, 2020). Particles will rebound off the capture surface if they remain physically intact on impact and have sufficient kinetic energy to overcome stiction forces. Thus, ice particles that do not melt or disrupt on impact simply bounce off the CS leading to a decline in observed organic capture efficiency. It is therefore reasonable to assume that a CS with greater sticking potential, such as a more pliable or frozen surface, will provide higher organic capture at low velocity. The perpendicular, vertical target placement in these experiments investigated only particle size and velocity effects on primary impacts on an indium capture surface, and therefore may be regarded as conservative estimates of plume capture capability. The vertical target placement used here allows weakly adhering particles to simply fall off (New et al. 2020)—a loss mechanism that does not occur in a 0 g environment.

The melting process of impacting ice particles may also be an important factor in determining the presence or absence of low-velocity residues. Gault and Heitowitz (1963) found that energy is approximately distributed evenly between the target and projectile during an impact and that the energy in the projectile dissipates via heating and physical deformation. To explore this model, we calculate how much energy is transferred to a 12.5 μm diameter ice particle on impact as a function of velocity and compare this to the amount of energy required to melt the particle (Fig. 10). The results indicate that particles with velocities below ~1.2 km s⁻¹ have insufficient energy to melt on impact and may rebound leading to less organic capture. This can be approximated by equating the phase change energy (mL) to half the kinetic energy ($\frac{1}{4}mv^2$), which yields $v = \sqrt[4]{4L}$. The latent heat of ice is $334 \times 10^3 \text{ J kg}^{-1}$ leading to a velocity of 1.16 km s⁻¹. This calculation neglects the comparatively small amount of energy required to raise the particle temperature prior to melting. Thus, this mechanism would predict a decrease in organic capture efficiency below the lower velocity limit of our experiments.

The two forms of PB residue in Fig. 5 indicate that there are variations in the nature of the impacting

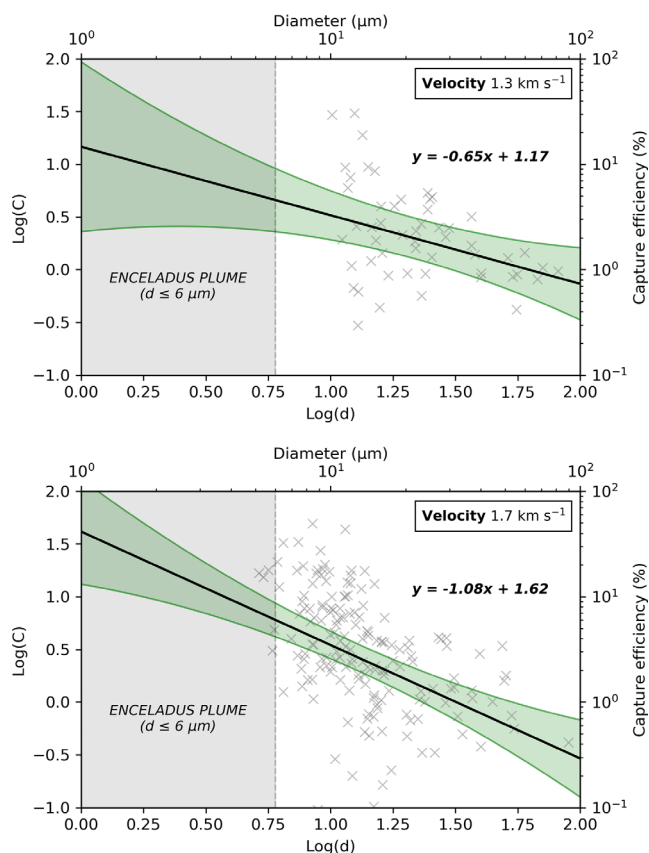


Fig. 9. Organic capture efficiency plotted against diameter for impacts at 1.3 and 1.7 km s⁻¹. The indicated functions (black line) have been fit to the data to estimate efficiencies for smaller particles. The green shading indicates the confidence bands (0.05 significance) of the fit and the gray-shaded region highlight the size of Enceladus plume particles at an altitude of 50 km. (Color figure can be viewed at wileyonlinelibrary.com.)

particles. While the crater residue is a result of high-density ice (HDI) particles that impact the foil, form craters, and deposit organic residue, the mechanism responsible for surface residue is less clear. One possibility is that at low velocities (10⁰–10² m s⁻¹), below the rebound velocity threshold where kinetic energy is insufficient to overcome surface tension, whole particles will stick to the capture surface and form highly saturated PB deposits independent of craters. Experimentally this might occur due to low-velocity trailing particles that escape the driver sabot. Alternatively, this phenomenon could be a result of low-density ice (LDI) particles impacting the foil and undergoing a similar PB deposition process. To minimize the uncertainty surrounding surface residue, we exclusively analyzed residue deposited in craters formed by HDI particles. We do, however, note that Enceladus plume particles may be porous, fluffy, or otherwise low density and that by neglecting these

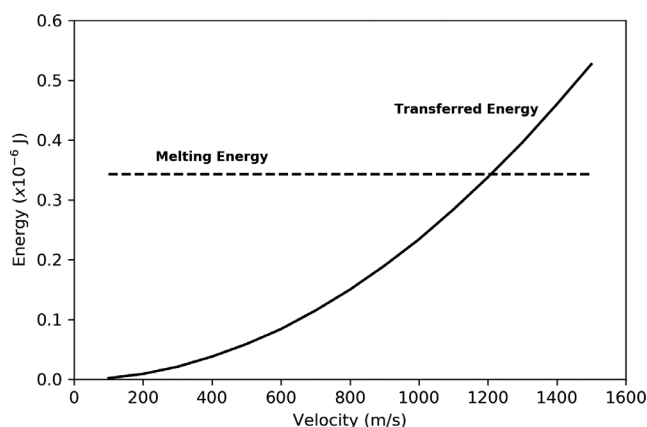


Fig. 10. Energy (μJ) required to melt a 12.5 μm diameter ice particle (dashed line) and the energy (μJ) transferred to the particle on impact (solid line) at different velocities (m s⁻¹).

impacts, we are presenting a lower bound for capture efficiency.

Our results highlight the feasibility of collecting unmodified organic molecules from the Enceladus plume for analysis. Organic capture efficiencies demonstrated in our experiments will allow us to reach sub-ppb sensitivity for organics when coupled to modern in situ analysis instrumentation such as microfluidic CE. Additional plume transects and further optimization of organic capture should provide enhanced total material capture providing lower ppb detection limits, illustrating an advantage of integrative capture chemical analysis over time-of-flight spectrometry where it is difficult to improve sensitivity with additional plume transects.

CONCLUSION

Collecting intact organic molecules in ice particles during Enceladus plume transects has been identified as a potential method of sampling unmodified subsurface ocean constituents for in situ chemical and biosignature analysis. While the analysis presented here concentrated on individual craters, at Enceladus, the organic biomarkers captured on our metal capture surface would be dissolved in a solution and transported to the analyzer. Collection of intact molecular biosignatures on a capture surface, when coupled with an appropriate sample dissolution and delivery method, is essential for a number of analytical techniques, including CE (e.g., EOA), spectroscopy, microscopy, or variants of chromatography-mass spectrometry. In contrast to time-of-flight mass spectrometry measurements, intact organic capture allows for the repetitive accumulation and harvesting of larger plume samples in order to increase the detection sensitivity of concentration-based chemical analyzers.

Our goal was to carry out impact experiments to determine the efficacy of our capture system under realistic impact conditions, as well as to probe the extent of impact degradation of complex organic molecules. The results clearly demonstrate that an indium surface can provide successful capture of intact organic molecules entrained in high-velocity ($1\text{--}2\text{ km s}^{-1}$) ice particles ($d < 15\text{ }\mu\text{m}$) and that capture efficiencies of $\sim 10\%$ can be expected when integrating over a large number of impacts, with capture as high as $\sim 50\%$ for individual impacts.

With the current data set, the optimal velocity is seen between 1 and 2 km s^{-1} where high organic capture efficiencies ($10\text{--}50\%$) are observed in over 25% of craters formed by small particles ($5\text{--}15\text{ }\mu\text{m}$). Capture efficiencies of $\sim 10\%$ are expected when integrating over all impacts. Under these impact conditions, entrained organic molecules remain chemically intact and deposit residue on the capture surface, which can be dissolved for later analysis. Organic capture decreases by at least an order of magnitude as the impact velocity approaches 3 km s^{-1} . Thus, any mission designed to collect samples from the plumes of Enceladus must consider the role of encounter velocity in determining the science measurement capabilities. For example, modeled after the ELF Mission proposal (Reh et al. 2016), a plume-pass velocity of $1\text{--}2\text{ km s}^{-1}$ can be achieved with a Saturn orbiter that has a very useful Enceladus close approach trajectory (Mathies et al. 2019).

These results are an important development for the design of future Enceladus missions supporting the hypothesis that pristine ocean constituents can be effectively sampled for organic analyses via plume transects. A remaining critical question is the exploration of capture surfaces that would be appropriate for an Enceladus orbiter, where the encounter velocities are only a few 100 m/s . In future work, we plan to study organic capture efficiencies for smaller particles with a wider velocity range and additional capture surfaces.

Acknowledgments—This work was made possible by funding from the National Aeronautics and Space Administration (NASA) under Grant No. 80NSSC17K0600 issued by the SMD/Planetary Science Division through the MatISSE Program. Richard Mathies thanks the UC Retirement System for financial support during the course of the project. The authors declare that they do not have any conflicts of interest. We thank the two anonymous reviewers who helped improve and clarify this manuscript.

Editorial Handling—Dr. Daniel Glavin

REFERENCES

- Abramoff M. D., Magalhães P. J., and Ram S. J. 2004. Image processing with ImageJ. *Biophotonics International* 11:36–42.
- Bowden S. A., Parnell J., and Burchell M. J. 2009. Survival of organic compounds in ejecta from hypervelocity impacts on ice. *International Journal of Astrobiology* 8:19–25.
- Burchell M. J., Cole M. J., McDonnell J. A. M., and Zarnecki J. C. 1999. Hypervelocity impact studies using the 2 MV Van de Graaff accelerator and two-stage light gas gun of the University of Kent at Canterbury. *Measurement Science and Technology* 10:41.
- Burchell M. J., Bowden S. A., Cole M., Price M. C., and Parnell J. 2014. Survival of organic materials in hypervelocity impacts of ice on sand, ice, and water in the laboratory. *Astrobiology* 14:473–485.
- Cao D., Liu Z., Verwilt P., Koo S., Jangjili P., Kim J. S., and Lin W. 2019. Coumarin-based small-molecule fluorescent chemosensors. *Chemical Reviews* 119:10403–10519.
- Chiesl T. N., Chu W. K., Stockton A. M., Amashukeli X., Grunthaner F., and Mathies R. A. 2009. Enhanced amine and amino acid analysis using Pacific Blue and the Mars Organic Analyzer microchip capillary electrophoresis system. *Analytical Chemistry* 81:2537–2544.
- Eichhorn G. 1978. Primary velocity dependence of impact ejecta parameters. *Planetary and Space Science* 26:469–471.
- Elsila J. E., Glavin D. P., and Dworkin J. P. 2009. Cometary glycine detected in samples returned by Stardust. *Meteoritics & Planetary Science* 44:1323–1330.
- Gault D. E. and Heitowit E. D. 1963. The partition of energy for hypervelocity impact craters formed in rock. *Proceedings of the Sixth Symposium on Hypervelocity Impact* 2:419–456.
- Glavin D. P., Dworkin J. P., and Sandford S. A. 2008. Detection of cometary amines in samples returned by Stardust. *Meteoritics & Planetary Science* 43:399–413.
- Glein C. R. and Zolotov M. Y. 2020. Hydrogen, hydrocarbons, and habitability across the solar system. *Elements: An International Magazine of Mineralogy, Geochemistry, and Petrology* 16:47–52.
- Hedman M. M., Nicholson P. D., Showalter M. R., Brown R. H., Buratti B. J., and Clark R. N. 2009. Spectral observations of the Enceladus plume with Cassini-VIMS. *The Astrophysical Journal* 693:1749.
- Hibbert R., Cole M. J., Price M. C., and Burchell M. J. 2017. The hypervelocity impact facility at the University of Kent: Recent upgrades and specialized capabilities. *Procedia Engineering* 204:208–214.
- Hsu H. W., Postberg F., Sekine Y., Shibuya T., Kempf S., Horányi M., Juhász A., Altobelli N., Suzuki K., Masaki Y., and Kuwatani T. 2015. Ongoing hydrothermal activities within Enceladus. *Nature* 519:207.
- Iess L., Stevenson D. J., Parisi M., Hemingway D., Jacobson R. A., Lunine J. I., Nimmo F., Armstrong J. W., Asmar S. W., Ducci M., and Tortora P. 2014. The gravity field and interior structure of Enceladus. *Science* 344:78–80.
- Khawaja N., Postberg F., Hillier J., Klenner F., Kempf S., Nölle L., Reviol R., Zou Z., and Srama R. 2019. Low-mass nitrogen-, oxygen-bearing, and aromatic compounds in Enceladean ice grains. *Monthly Notices of the Royal Astronomical Society* 489:5231–5243.
- Klenner F., Postberg F., Hillier J., Khawaja N., Reviol R., Stolz F., Cable M. L., Abel B., and Nölle L. 2020. Analog

- experiments for the identification of trace biosignatures in ice grains from extraterrestrial ocean worlds. *Astrobiology* 20:179–189.
- Lunine J. I. 2017. Enceladus and its plume. *Nature Astronomy* 1:581.
- Mathies R. A., Razu M. E., Kim J., Stockton A. M., Turin P., and Butterworth A. L. 2017. Feasibility of detecting bioorganic compounds in Enceladus plumes with the Enceladus Organic Analyzer. *Astrobiology* 17:902–912.
- Mathies R. A., New J. S., Golozar M., McCauley J., and Butterworth A. L. 2019. Evaluation of science measurement capabilities for Enceladus plume fly-by flight profiles based on experimental hypervelocity particle impact studies and Enceladus Organic Analyzer (EOA) sample analysis capabilities (abstract #P24A-08). AGU Fall Meeting Abstracts, Special Session on Enceladus.
- McKay C. P., Porco C. C., Altheide T., Davis W. L., and Kral T. A. 2008. The possible origin and persistence of life on Enceladus and detection of biomarkers in the plume. *Astrobiology* 8:909–919.
- New J. S., Mathies R. A., Butterworth A. L., Price M. C., Kazemi B., Spathis V., and Golozar M. 2019. Hypervelocity Particle Capture on Inert Metal Substrates: Foundations for organic particle capture and analysis of Enceladus plume transects (abstract #P21D–3414). AGU Fall Meeting Abstracts.
- New J. S., Mathies R. A., Price M. C., Cole M. J., Golozar M., Spathis V., Burchell M. J., and Butterworth A. L. 2020. Characterizing organic particle impacts on inert metal surfaces: Foundations for capturing organic molecules during hypervelocity transits of Enceladus plumes. *Meteoritics & Planetary Science* 55:465–479.
- Pavlov A., McLain H. L., Glavin D. P., Dworkin J. P., Elsila C. J., and House C. H. 2019. Degradation of the biomolecules in Europa-like ice conditions due to exposure to ionizing radiation. (abstract #P52B–08). AGU Fall Meeting Abstracts.
- Pérez-González A., Rebollar-Zepeda A. M., León-Carmona J. R., and Galano A. 2012. Reactivity indexes and OH bond dissociation energies of a large series of polyphenols: Implications for their free radical scavenging activity. *Journal of the Mexican Chemical Society* 56:241–249.
- Porco C. C., Helfenstein P., Thomas P. C., Ingersoll A. P., Wisdom J., West R., Neukum G., Denk T., Wagner R., Roatsch T., and Kieffer S. 2006. Cassini observes the active south pole of Enceladus. *Science* 311:1393–1401.
- Porco C. C., Dones L., and Mitchell C. 2017. Could it be snowing microbes on Enceladus? Assessing conditions in its plume and implications for future missions. *Astrobiology* 17:876–901.
- Postberg F., Kempf S., Hillier J. K., Srama R., Green S. F., McBride N., and Grün E. 2008. The E-ring in the vicinity of Enceladus: II. Probing the moon's interior—The composition of E-ring particles. *Icarus* 193:438–454.
- Postberg F., Kempf S., Schmidt J., Brilliantov N., Beinsen A., Abel B., Buck U., and Srama R. 2009. Sodium salts in E-ring ice grains from an ocean below the surface of Enceladus. *Nature* 459:1098.
- Postberg F., Schmidt J., Hillier J., Kempf S., and Srama R. 2011. A salt-water reservoir as the source of a compositionally stratified plume on Enceladus. *Nature* 474:620.
- Postberg F., Khawaja N., Abel B., Choblet G., Glein C. R., Gudipati M. S., Henderson B. L., Hsu H. W., Kempf S., Klenner F., and Moragas-Klostermeyer G. 2018. Macromolecular organic compounds from the depths of Enceladus. *Nature* 558:564.
- Reh K., Spilker L., Lunine J. I., Waite J. H., Cable M. L., Postberg F., and Clark K. 2016. Enceladus Life Finder: The search for life in a habitable Moon. *IEEE Aerospace Conference*. <https://doi.org/10.1109/AERO.2016.7500813>
- Sekine Y., Shibuya T., Postberg F., Hsu H. W., Suzuki K., Masaki Y., Kuwatani T., Mori M., Hong P. K., Yoshizaki M., and Tachibana S. 2015. High-temperature water–rock interactions and hydrothermal environments in the chondrite-like core of Enceladus. *Nature Communications* 6:1–8.
- Skelly A. M., Scherer J. R., Aubrey A. D., Grover W. H., Ivester R. H., Ehrenfreund P., Grunthaner F. J., Bada J. L., and Mathies R. A. 2005. Development and evaluation of a microdevice for amino acid biomarker detection and analysis on Mars. *Proceedings of the National Academy of Sciences of the United States of America* 102:1041–1046.
- Skelly A. M., Aubrey A. D., Willis P. A., Amashukeli X., Ehrenfreund P., Bada J. L., Grunthaner F. J., and Mathies R. A. 2007. Organic amine biomarker detection in the Yungay region of the Atacama Desert with the Urey instrument. *Journal of Geophysical Research: Biogeosciences* 112.
- Spahn F., Schmidt J., Albers N., Hörning M., Makuch M., Seiß M., Kempf S., Srama R., Dikarev V., Helfert S., and Moragas-Klostermeyer G. 2006. Cassini dust measurements at Enceladus and implications for the origin of the E ring. *Science* 311:1416–1418.
- Spencer J. R., Pearl J. C., Segura M., Flasar F. M., Mamoutkine A., Romani P., Buratti B. J., Hendrix A. R., Spilker L. J., and Lopes R. M. C. 2006. Cassini encounters Enceladus: Background and the discovery of a south polar hot spot. *Science* 311:1401–1405.
- Thomas P. C., Tajeddine R., Tiscareno M. S., Burns J. A., Joseph J., Loredo T. J., Helfenstein P., and Porco C. 2016. Enceladus's measured physical libration requires a global subsurface ocean. *Icarus* 264:37–47.
- Waite J. H., Combi M. R., Ip W. H., Cravens T. E., McNutt R. L., Kasprzak W., Yelle R., Luhmann J., Niemann H., Gell D., and Magee B. 2006. Cassini ion and neutral mass spectrometer: Enceladus plume composition and structure. *Science* 311:1419–1422.
- Waite J. H., Lewis W. S., Magee B. A., Lunine J. I., McKinnon W. B., Glein C. R., Mousis O., Young D. T., Brockwell T., Westlake J., and Nguyen M. J. 2009. Liquid water on Enceladus from observations of ammonia and ⁴⁰Ar in the plume. *Nature* 460:487.
- Waite J. H., Glein C. R., Perryman R. S., Teolis B. D., Magee B. A., Miller G., Grimes J., Perry M. E., Miller K. E., Bouquet A., and Lunine J. I. 2017. Cassini finds molecular hydrogen in the Enceladus plume: Evidence for hydrothermal processes. *Science* 356:155–159.
- Waller S. E., Tallarida N., Lambert J. L., Belousov A. E., Madzunkov S. M., Darrach M., Hodyss R. P., Malaska M., Hofmann A., Charvat A., and Abel B. 2019. Analyzing Enceladus' plume constituents: First steps to experimentally simulating hypervelocity impacts (abstract #P24A–07) AGU Fall Meeting Abstracts.